Energy & Environmental Science

ROYAL SOCIETY OF CHEMISTRY

PAPER

View Article Online
View Journal | View Issue

Cite this: *Energy Environ. Sci.*, 2021, **14**, 1584

Photogeneration and the bulk quantum efficiency of organic photovoltaics†

Kan Ding,[a] Xiaheng Huang,[b] Yongxi Li[b] and Stephen R. Forrest *[abc]

Received 11th December 2020,
Accepted 17th February 2021

DOI: 10.1039/d0ee03885g

rsc.li/ees

We introduce a method to analyze the performance of bulk heterojunction (BHJ) organic photovoltaics (OPVs) by calculating its "bulk quantum efficiency" (BQE), a quantity related to the recombination losses within the BHJ, but not in the surrounding device layers. By applying the method to both vacuum- and solution-processed OPVs with various BHJ, buffer layers and interface layer compositions, we show that measurements of the BQE isolates the properties of the BHJ from other device layers and interfaces. We use measurements of the BQE to study various mechanisms in OPV degradation and find that for solution-processed OPVs with a ZnO cathode buffer layer, the BHJ undergoes degradation due primarily to the ZnO. By inserting a self-assembled monolayer at the interface between the buffer and the BHJ, the stability of the OPV is significantly improved.

1. Introduction

Bulk heterojunctions (BHJs) are isotropic mixtures of donor and acceptor molecules that conventionally serve as active layers in organic photovoltaics (OPVs) due to their advantage of circumventing the tradeoff between the short exciton diffusion lengths (usually <20 nm) and long optical absorption lengths (usually >50 nm) of organic materials.[1–5] Diode rectification characteristics are therefore a result of inclusion of carrier-selective buffer layers between the BHJ and the contacts.[6,7] Due to the localized nature of absorption and charge recombination,[8–12] conventional metrics of OPV performance, *i.e.*, open-circuit voltage (V_{OC}), short-circuit current density (J_{SC}) and fill factor (FF), can provide only limited physical insights into the photogeneration processes in OPVs.[13–18]

In this work, we introduce a convenient method to analyze the performance and aging of OPV devices by calculating the photogeneration efficiency of the BHJ itself, called the bulk quantum efficiency (BQE), which is independent of the contacts, buffer layers and their interfaces (so-called device edges) within the structure. This quantity enables the separate evaluation and ultimately the optimization of the BHJ and edges, and directly reveals the various mechanisms responsible for OPV degradation during extended operation. The validity of the use of BQE device analysis is tested against experimental results of both vacuum- and solution-processed OPVs with a variety of BHJs, buffer layers and interface layer compositions. It is found that in solution-processed OPVs with a ZnO cathode buffer layer (CBL), the buffer is primarily responsible for loss of photogeneration efficiency over time. A self-assembled monolayer (SAM) inserted at the ZnO/BHJ interface suppresses degradation, leading to a significantly improved device lifetime.

2. Theory

2.1 Derivation of BQE

The internal quantum efficiency (IQE) is defined as the ratio of the number of extracted photogenerated charge carrier pairs to the number of absorbed photons. The IQE is less than unity in the presence of recombination. If the charge carriers are localized, the IQE can written as:

$$\mathrm{IQE}(V) = \frac{J_{\mathrm{ph}}(V)}{q\Phi\eta_{\mathrm{abs}}} = \left(1 - r_{\mathrm{bulk}}(V_{\mathrm{bulk}})\right) \cdot \left(1 - r_{\mathrm{edge}}\left(V_{\mathrm{edge}}\right)\right), \quad (1)$$

where q is the elementary charge, Φ is the incident photon flux and η_{abs} is the absorption efficiency. Also, $J_{\mathrm{ph}}(V)$ is the photocurrent density at the applied voltage, V, and is equal to the difference between total current density, J_{tot}, and dark current, J_{dark}. The recombination efficiencies in the BHJ and at the edges are given by r_{bulk} and r_{edge}, with corresponding voltage drops V_{bulk} and V_{edge}, respectively. The V_{bulk} is the macroscopic voltage drop across the BHJ given by:

$$V_{\mathrm{bulk}} = -\int_0^D F(z)\mathrm{d}z, \quad (2)$$

[a] *Department of Physics, University of Michigan, Ann Arbor, MI 48109, USA. E-mail: stevefor@umich.edu*
[b] *Department of Electrical Engineering and Computer Science, University of Michigan, Ann Arbor, MI 48109, USA*
[c] *Departments of Material Science and Engineering, University of Michigan, Ann Arbor, MI 48109, USA*

† Electronic supplementary information (ESI) available. See DOI: 10.1039/d0ee03885g

where D is the BHJ thickness, z is the distance to the anode, and F is the average electric field component in the z direction. Due to the random orientation of the donor–acceptor interfaces in a BHJ, the local electric field direction can also be random, leading to nonuniformities in $F(z)$. But F should be monotonic and point from the cathode to the anode for efficient charge extraction to occur. We assume the charge recombination only depends on the local electric field. This assumption can be invalid when the density of photogenerated charges is high, as discussed further in ESI.† The first term, $(1 - r_{\text{bulk}}(V_{\text{bulk}}))$, is the BQE. We write V_{edge} as:

$$V_{\text{edge}} = V_{\text{int}} + AJ_{\text{tot}}R_{\text{edge}}, \tag{3}$$

where V_{int} is the sum of voltages across various interfaces, R_{edge} is the sum of the resistances of all edge layers, and A is the device area. To proceed, two assumptions are made: (i) $r_{\text{bulk}} \approx 0$ when V_{bulk} is large; (ii) $AJ_{\text{tot}}\,R_{\text{edge}} \ll V_{\text{int}}$, where the dependence of V_{int} on applied voltage is much smaller than V_{bulk}. This latter assumption is based on the understanding that V_{int} is primarily due to dipoles resulting from the work function difference across the interface. On the other hand, this may not be correct in the presence of a large, mid-energy gap interfacial trap state density.[19–22] Assumption (i) results since both geminate and non-geminate recombination vanish at high electric fields.[23–25] Assumption (ii) requires the buffer layers to have low resistance compared to the bulk (which is a combination of the junction and internal layer resistances). Therefore, at large reverse bias, eqn (1) becomes:

$$\text{IQE}|_{-V\to\text{large}} = \frac{J_{\text{sat}}}{q\Phi\eta_{\text{abs}}} \approx 1 - r_{\text{edge}}(V_{\text{edge}}), \tag{4}$$

where J_{sat} is the saturated photocurrent density at large reverse bias. Then, using eqn (1) and (4):

$$\text{BQE}(V_{\text{bulk}}) = (1 - r_{\text{bulk}}(V_{\text{bulk}})) \approx \frac{\text{IQE}(V)}{\text{IQE}|_{-V\to\text{large}}} = \frac{J_{\text{ph}}(V)}{J_{\text{sat}}}. \tag{5}$$

This quantity is the charge collection probability, or normalized photocurrent that has been previously introduced.[26,27] In this work we show that BQE is the quantum efficiency specific only to the BHJ, and is independent of the edges in the device. Although BQE is expected to depend on light intensity when high order events (*e.g.*, exciton–exciton annihilation) or charge accumulation are present, we find BQE(V_{bulk}) is almost independent of intensity at 100 mW cm^{-2} or lower in the junctions studied (see ESI†).

Fig. 1 shows the energy level diagram of an OPV under a forward bias of $V < V_{\text{OC}}$ with a schematic indicating the direction of photogenerated current flow. We assume the hole quasi-Fermi level (E_{Fh}) is pinned at δ_1 above the highest occupied molecular orbital (HOMO) level of the donor on the anode side (E_{D}), and electron quasi-Fermi level (E_{Fe}) is pinned at δ_2 below the lowest unoccupied molecular orbital (LUMO) level of the acceptor on the cathode side (E_{A}). Then:

$$qV = E_{\text{Fe}} - E_{\text{Fh}} = (E_{\text{A}} - \delta_2) - (E_{\text{D}} - \delta_1) = \Delta E_{\text{HL}} - qV_{\text{edge}} - qV_{\text{bulk}}, \tag{6}$$

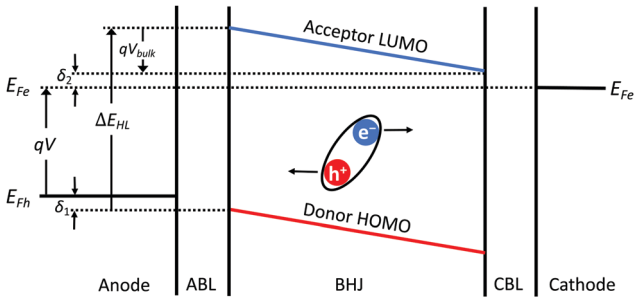

Fig. 1 Energy level diagram of an OPV under forward bias that is smaller than the open-circuit voltage. The hole quasi-Fermi energy, E_{Fh}, is pinned at δ_1 above the donor HOMO level on the anode side, while the electron quasi-Fermi energy, E_{Fe}, is at δ_2 below the acceptor LUMO level on the cathode side.

where ΔE_{HL} is the energy offset between the acceptor LUMO and the donor HOMO, and $V_{\text{edge}} = \delta_1 + \delta_2$. For convenience, the $V_{\text{bulk}} > 0$ is defined as opposite to that of V, since V_{bulk} and V have opposite signs under OPV operation.

To understand the relationship between the applied voltage, V, and V_{bulk}, we assume in an ideal OPV that all contacts are ohmic and $V_{\text{edge}} = 0$. Fig. 2a shows the energy level diagram of the ideal OPV under reverse bias, $V < 0$. According to eqn (6), $V_{\text{bulk}} = \Delta E_{\text{HL}}/q + |V|$. At short-circuit, as shown in Fig. 2b, $V = 0$ and $V_{\text{bulk}} = \Delta E_{\text{HL}}$. Under the solar cell working conditions, $V > 0$ and $V_{\text{bulk}} = \Delta E_{\text{HL}}/q - V$, as shown in Fig. 2c, and Fig. 2d shows the condition when there is no electric field in the BHJ, in which case $V = \Delta E_{\text{HL}}/q$, $V_{\text{bulk}} = 0$.

Due to the random orientation of dissociating interfaces and localized charge states in the BHJ, photogenerated charge suffer increased recombination losses compared with planar junctions. Under the condition in Fig. 2d, there is no electric field in the BHJ to help photogenerated charges overcome their Coulomb attraction and guide them towards their respective electrodes. In this case, the probability for the charges to contribute to the photocurrent is low. Here, we approximate $J_{\text{ph}} = 0$ when $V_{\text{bulk}} = 0$. This assumption is invalid for spatially regular junctions (*e.g.*, a bilayer structure), leading to diffusion dominated photocurrent, or the charges experience band-like transport with no recombination loss (*e.g.*, inorganic semiconductors), or the photogenerated charge density is high and forms a density gradient throughout the BHJ. In this case, eqn (6) becomes:

$$V|_{J_{\text{ph}}=0} = V_{\text{off}} = \frac{\Delta E_{\text{HL}}}{q} - V_{\text{edge}}, \tag{7}$$

where we rename $V|_{J_{\text{ph}}=0}$ as V_{off}, referring to the offset voltage between V and V_{bulk}. Using eqn (6) and (7), we obtain:

$$V_{\text{bulk}} = V_{\text{off}} - V. \tag{8}$$

Note that although eqn (4) and (7) are helpful for understanding the physical origins of J_{sat} and V_{off}, BQE(V_{bulk}) can be directly obtained from J_{ph}(V) through eqn (5) and (8). Step-by-step guidance to calculating BQE(V_{bulk}) is provided in ESI.†

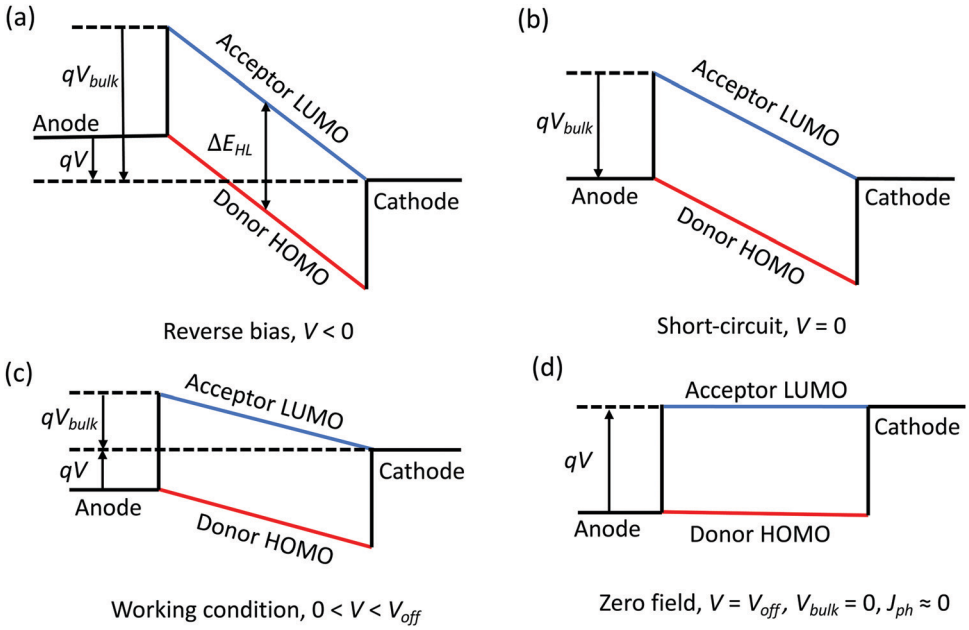

Fig. 2 (a) Energy level diagram of an OPV with ohmic contacts under reverse bias. (b) Energy level diagram of the OPV at short-circuit, (c) under solar cell working conditions, and (d) when there is no electric field across the BHJ.

To sum up, our theory rests on three assumptions: (i) $r_{bulk} \approx 0$ when V_{bulk} is large; (ii) the dependence of V_{int} on applied voltage is much smaller than V_{bulk}; (iii) when $V_{bulk} = 0, J_{ph} = 0$. When these assumptions are valid, then BQE(V_{bulk}) is a property of the BHJ alone, and consequently is independent of other layers and interfaces within the device. Recombination outside of the BHJ affects J_{sat} as shown in eqn (4), while voltage drops outside the BHJ affect V_{off} as in eqn (7).

2.2 BQE degradation equation due to a low concentration of traps

As an OPV ages, its BQE decreases. To understand the aging process, we assume that conductivity within the BHJ is due to thermally-assisted hopping, and that trap sites with energy ΔE_t within the energy gap are generated over time. The thermal activated rate for a charge to escape a trap site, k_{esc}, is:[28]

$$k_{esc} = k_0 \exp\left(-\frac{\Delta E_t}{kT}\right), \quad (9)$$

where k_0 is a constant, k is the Boltzmann constant and T is the temperature. In an electric field, F, the energy barrier for thermal activation is lowered to $\Delta E_t - qFd$, where d is the distance between neighboring sites. Assuming a uniform electric field in a BHJ of thickness D, then $F = V_{bulk}/D$. The probability for a trapped charge to recombine is then:

$$P_{rec} = \frac{k_{rec}}{k_{rec} + k_{esc}} = \frac{k_{rec}}{k_{rec} + k_0 \exp\left(-\frac{\Delta E_t - qV_{bulk}d/D}{kT}\right)}, \quad (10)$$

where k_{rec} is the recombination rate of trapped charges. In the low trap site density limit where every photogenerated charge gets trapped at most once prior to extraction, the decrease in BQE is:

$$\Delta BQE = BQE_0 P_{trap} P_{rec} = BQE_0 P_{trap} \frac{k_{rec}}{k_{rec} + k_0 \exp\left(-\frac{\Delta E_t - \frac{qV_{bulk}d}{D}}{kT}\right)} = BQE_0 \left[\frac{P_{trap}}{1 + C_{esc}\exp(V_{bulk}/V_{esc})}\right], \quad (11)$$

where BQE_0 is the BQE of the unaged device, and P_{trap} is the probability for photogenerated charges to become trapped during extraction. Also:

$$C_{esc} = \frac{k_0}{k_{rec}} \exp\left(-\frac{\Delta E_t}{kT}\right), \quad (12a)$$

and

$$V_{esc} = \frac{kTD}{qd}. \quad (12b)$$

Here, the escape constant, C_{esc}, is the ratio of the escape to the recombination rate at zero electric field, and V_{esc} is the escape voltage. It follows that for efficient charge extraction, V_{bulk} must be larger than V_{esc}. Note that eqn (11) is derived in the low trap density limit and does not include other degradation mechanisms such as morphological changes over time.

3. Results

To test that BQE(V_{bulk}) depends only on photogeneration originating in the BHJ, OPV devices with various BHJs, buffer

layers and interface qualities are fabricated. Fig. 3a shows the BQE–V_{bulk} characteristics of OPVs with identical BHJs comprising DBP as the donor and C_{70} as the acceptor, but with a variety of anode buffer layers (ABLs). The device structures are: ITO 150 nm/ABL 10 nm/DBP : C_{70}, 1 : 8, 54 nm/BPhen 7 nm/Ag 100 nm as shown in the inset. For ease in comparing the BQE–V_{bulk} data, we define V_{80} as the V_{bulk} required to achieve a BQE of 80%, *i.e.*:

$$V_{80} = V_{bulk}|_{BQE=80\%}, \quad (13)$$

The charge extraction from a BHJ is more efficient when V_{80} is small. The V_{80} along with V_{off}, J_{sat} and power conversion efficiencies (PCEs) are provided in Table 1. The BHJ itself has been reported to be highly stable under intense sunlight exposure, albeit with different cathode and anode buffers than used here.[29] Full chemical names, chemical structures and frontier orbital energies of materials used in this work can be found in ESI.† The *J*–*V* characteristics of each device are shown in Fig. 3b. Although V_{OC}, J_{SC} and FF depend on the choice of ABL, their BQE–V_{bulk} characteristics are almost identical. With different ABLs, the V_{80} are similar, while V_{off} and J_{sat} vary significantly. The J_{sat} is chosen to equal J_{ph} at −1 V. The choice of J_{sat} affects the absolute value of BQE, but not the shape of the BQE–V_{bulk} characteristics (see ESI†).

Previously, it has been found that a thin anode interface layer (AIL) inserted between the ABL and BHJ determines the interface voltage, which contributes to V_{edge}.[19] Fig. 4a shows the BQE–V_{bulk} characteristics of OPVs with identical BHJs and a 3 nm-thick AIL of various materials. The device structures are: ITO 150 nm/MoO_x 10 nm/AIL 3 nm/DTDCPB:C_{70}, 1 : 2, 80 nm/BPhen 7 nm/Ag 100 nm as shown in the inset. The *J*–*V* characteristics of each device are shown in Fig. 4b, with V_{off}, J_{sat}, V_{80} and PCEs listed in Table 2. The V_{off} is a sensitive function of the AIL composition, although the BQE–V_{bulk} characteristics are similar due to the use of the same BHJ in each device.

As discussed in Section 2.1, a planar junction can lead to a non-zero J_{ph} even when V_{bulk} = 0. To evaluate the effectiveness of the use of BQE under such conditions, OPVs with gradient mixing across the BHJs with MoO_x or HAT-CN ABLs are fabricated, with their BQE–V_{bulk} characteristics shown in Fig. 5a. The device structures are: ITO 150 nm/ABL 10 nm// DTDCPB:C_{70}, various gradient mixing ratios, 80 nm/BPhen 7 nm/Ag 100 nm, as shown in the inset. The gradients in C_{70} concentrations in the legend are from the anode to the cathode side. The *J*–*V* characteristics are shown in Fig. 5b, with device parameters provided in Table 3. The BQE–V_{bulk} characteristics are same for devices with similar gradient mixing ratios, while J_{sat}, V_{off} and PCEs vary for different ABLs. The results indicate that the BQE analysis still separates the bulk from edges in such inhomogeneous BHJs.

Table 1 Device characteristics of OPVs with a DBP:C_{70} BHJ and various anode buffer layer (ABL) materials

ABL material	V_{off} (V)	J_{sat} (mA cm^{-2})	V_{80} (V)	PCE (%)
WO_x	0.50 ± 0.01	12.9 ± 0.3	0.43 ± 0.03	2.5 ± 0.3
PEDOT:PSS	0.99 ± 0.01	15.0 ± 0.3	0.46 ± 0.03	7.2 ± 0.3
HAT-CN	0.63 ± 0.01	13.7 ± 0.3	0.48 ± 0.03	4.1 ± 0.2
MoO_x	0.97 ± 0.01	13.8 ± 0.3	0.44 ± 0.03	5.5 ± 0.2

We also determined the BQE of solution-processed, inverted OPVs with PCE-10 as the donor and BT-CIC as the acceptor.[30,31] Fig. 6a shows BQE–V_{bulk} characteristics of the OPVs with two different CBLs (ZnO and SnO_2) and various AILs. The device structures are: ITO 150 nm/CBL 30 nm/PCE-10 : BT-CIC, 1 : 1.5, 80 nm/AIL 3 nm/MoO_x 10 nm/Al 100 nm as shown in the inset. Their *J*–*V* characteristics are shown in Fig. 6b, and device parameters are provided in Table 4. Again, all devices have almost identical BQE–V_{bulk} characteristics. The OPV with a SnO_2 CBL has J_{sat} that is 3 mA cm^{-2} smaller than that with a ZnO CBL, while various AILs primarily affect V_{off}.

Fig. 7a shows the BQE–V_{bulk} characteristics of an OPV with DBP:C_{70} BHJ aged under a white light-emitting diode (LED) array which delivers an equivalent intensity of 27 suns (27 kW m^{-2}, lacking UV content).[29] The inset shows V_{80} *vs.* aging time. The device structure is: ITO 150 nm/MoO_x 10 nm/DBP : C_{70}, 1 : 8, 54 nm/C_{70} 9 nm/TPBi : C_{70}, 1 : 1, 10 nm/TPBi 3 nm/Ag 100 nm.

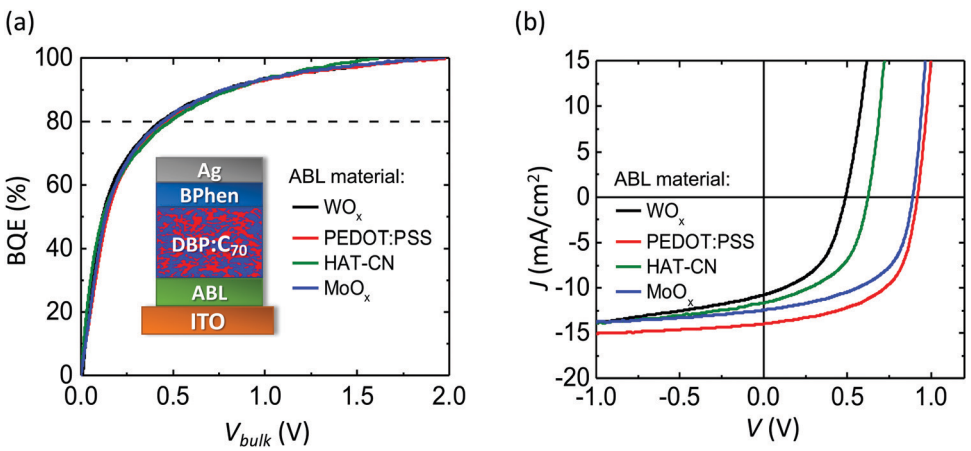

Fig. 3 (a) BQE–V_{bulk} characteristics of OPVs with identical bulk heterojunction (BHJ) layers of DBP as the donor and C_{70} as the acceptor (1 : 8 by volume, 54 nm thick), and various anode buffer layers (ABLs). Inset: Device structure. (b) Current density–voltage (*J*–*V*) characteristics of devices in (a).

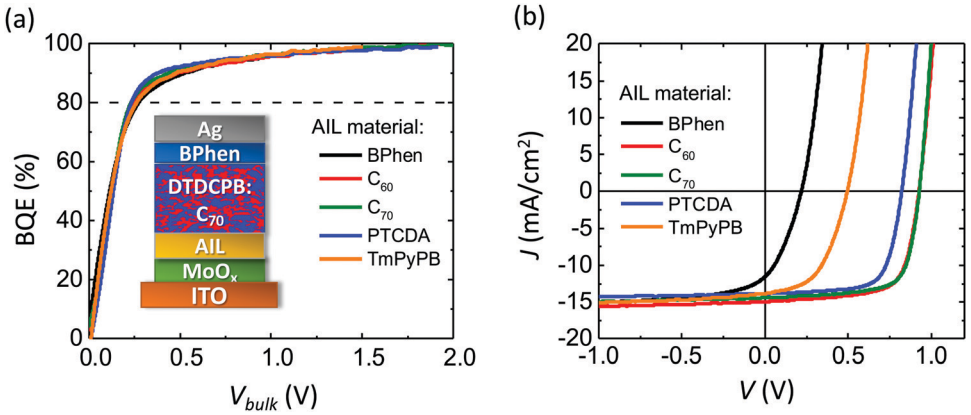

Fig. 4 (a) BQE–V_{bulk} characteristics of OPVs with identical BHJs comprising DTDCPB as the donor and C_{70} as the acceptor (1 : 2 by volume, 80 nm thick) and various anode interface layers (AILs). Inset: Device structure. (b) J–V characteristics of devices in (a).

Table 2 Device characteristics of OPVs with a DTDCPB:C_{70} BHJ and various anode interface layer (AIL) materials

AIL material	V_{off} (V)	J_{sat} (mA cm^{-2})	V_{80} (V)	PCE (%)
BPhen	0.22 ± 0.01	15.4 ± 0.3	0.27 ± 0.02	0.8 ± 0.1
C_{60}	1.02 ± 0.01	15.6 ± 0.3	0.24 ± 0.02	9.4 ± 0.2
C_{70}	1.05 ± 0.01	14.9 ± 0.3	0.23 ± 0.02	9.3 ± 0.2
PTCDA	0.94 ± 0.01	14.3 ± 0.3	0.22 ± 0.02	8.0 ± 0.2
TmPyPB	0.50 ± 0.01	15.3 ± 0.3	0.24 ± 0.02	3.4 ± 0.2

After 1000 h, V_{80} increases by approximately 0.2 V. The V_{off} and J_{sat} *vs.* time are shown in Fig. 7b. The V_{off} remains stable while J_{sat} decreases by approximately 10%.

Fig. 7c shows the change in BQE, ΔBQE, relative to the device prior to aging. The experimental (symbols) and results fit to eqn (11) (lines) are in reasonable agreement, assuming V_{esc} = 0.5 V, which corresponds to a site distance d = 4.1 nm. Values of fitting parameters, P_{trap}, C_{esc} and V_{esc}, for each line are provided in ESI.† Fig. 7d shows the maximum value of ΔBQE *vs.* aging time. Since ΔBQE ∝ P_{trap}, the results suggest that the trap site density increases linearly with time after an initial burn-in.

Table 3 Device characteristics of OPVs with gradient mixed DTDCPB:C_{70} BHJs and various anode buffer layers (ABL). The C_{70} concentrations are referenced from the anode to the cathode side

ABL material	C_{70} conc. (%)	V_{off} (V)	J_{sat} (mA cm^{-2})	V_{80} (V)	PCE (%)
MoO_x	40–60	0.85 ± 0.01	14.7 ± 0.3	0.24 ± 0.02	7.4 ± 0.1
HAT-CN	40–60	0.61 ± 0.01	14.3 ± 0.3	0.26 ± 0.02	4.0 ± 0.2
MoO_x	30–70	0.88 ± 0.01	14.1 ± 0.3	0.38 ± 0.02	7.1 ± 0.2
HAT-CN	30–70	0.36 ± 0.01	14.6 ± 0.3	0.42 ± 0.02	2.0 ± 0.2
MoO_x	20–80	0.91 ± 0.01	12.9 ± 0.3	0.62 ± 0.02	5.7 ± 0.2
HAT-CN	20–80	0.43 ± 0.01	11.7 ± 0.3	0.63 ± 0.02	1.7 ± 0.2

To separate the contributions of the MoO_x layer and the MoO_x/BHJ interface from the BHJ in the BQE decrease in Fig. 7a, the lower section of the OPV including the ITO layer, the MoO_x layer and 10 nm of the DBP:C_{70} BHJ were aged for 17 days under the same conditions as in Fig. 7a before the remaining layers are deposited (called the partly aged device), as shown in Fig. 8a. For comparison, a complete device with the same structure was fabricated (the as-grown device) and aged for the same amount of time at 27 suns (the fully aged device).

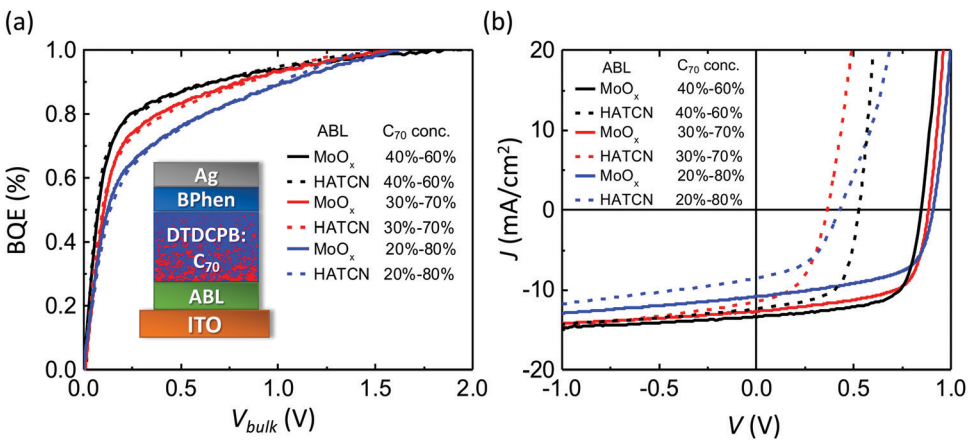

Fig. 5 (a) BQE–V_{bulk} characteristics of DTDCPB:C_{70} OPVs with gradient C_{70} concentrations from the anode to the cathode side (80 nm), and various anode buffer layers (ABLs). Inset: Device structure. (b) Current density–voltage (J–V) characteristics of devices in (a).

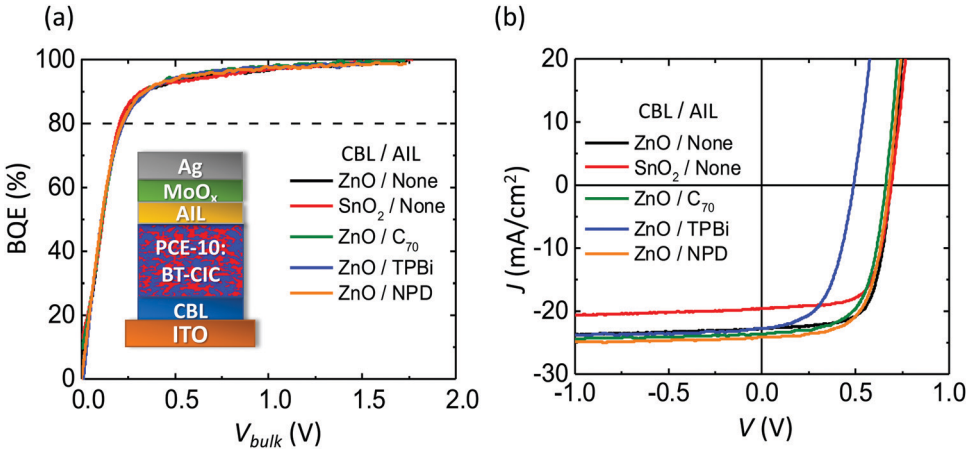

Fig. 6 (a) BQE–V_{bulk} characteristics of OPVs with identical BHJs of PCE-10 as the donor and BT-CIC as the acceptor (1 : 1.5 by weight, 80 nm thick) and various cathode buffer layer (CBL)/AIL compositions. Inset: Device structure. (b) J–V characteristics of devices in (a).

Table 4 Device characteristics of inverted OPVs with a PCE-10:BT-CIC BHJ and various cathode buffer layer (CBL) and AIL compositions

CBL/AIL	V_{off} (V)	J_{sat} (mA cm^{-2})	V_{80} (V)	PCE (%)
ZnO/none	0.74 ± 0.01	24.1 ± 0.3	0.21 ± 0.02	10.0 ± 0.2
SnO_2/none	0.77 ± 0.01	21.1 ± 0.3	0.22 ± 0.02	9.1 ± 0.2
ZnO/C_{70}	0.72 ± 0.01	24.3 ± 0.3	0.22 ± 0.02	9.7 ± 0.2
ZnO/TPBi	0.52 ± 0.01	24.0 ± 0.3	0.21 ± 0.02	5.9 ± 0.2
ZnO/NPD	0.74 ± 0.01	25.1 ± 0.3	0.21 ± 0.02	10.4 ± 0.2

The BQE–V_{bulk} characteristics of the partly aged device are compared with those of the as-grown device and the fully aged device, as shown in Fig. 8b. The device parameters of the unaged and aged devices are provided in Table 5. Although the MoO_x layer and the MoO_x/BHJ interface experience intense light exposure, the partly aged device has almost identical BQE–V_{bulk} characteristics as the as-grown device. The V_{off} and J_{sat} of the partly aged device, however, drop significantly.

Fig. 9a shows the BQE–V_{bulk} characteristics of an OPV aged under 1 sun intensity, simulated AM 1.5G illumination from a

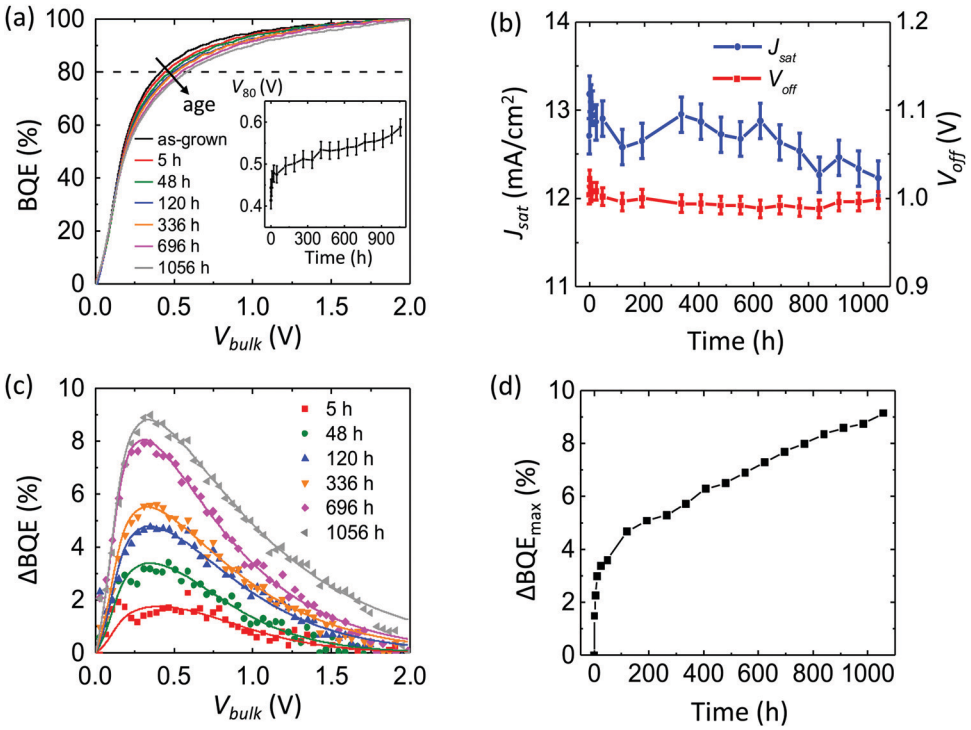

Fig. 7 (a) BQE–V_{bulk} characteristics of a DBP:C_{70} OPV aged under white light with an intensity equivalent to 27 suns. Inset: V_{80} *vs.* aging time. (b) V_{off} and J_{sat} *vs.* aging time. (c) Experimental (symbols) and fitted (lines) values of the decrease in BQE relative to the as-grown device (ΔBQE) *vs.* V_{bulk} at various aging times. (d) Maximum values of ΔBQE *vs.* aging time.

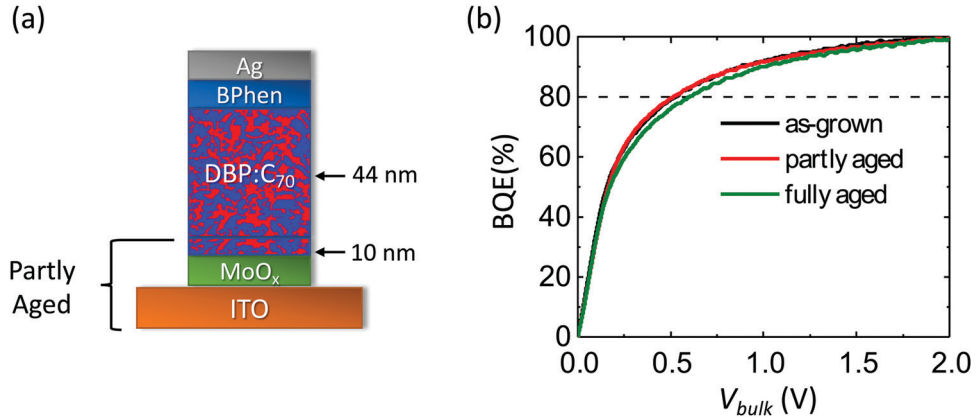

Fig. 8 (a) Structure of the partly aged and fully aged OPVs. The ITO layer, MoO_x layer and bottom 10 nm of the BHJ were aged under white light with an intensity equivalent to 27 suns for 17 days in the partly aged device. (b) BQE–V_{bulk} characteristics of the partly aged device, the as-grown device, and the fully aged device.

Table 5 Device characteristics of DBP:C_{70} OPVs with various aging procedures

Device	V_{off} (V)	J_{sat} (mA cm^{-2})	V_{80} (V)	PCE (%)
As-grown	0.94 ± 0.01	13.3 ± 0.3	0.52 ± 0.03	5.3 ± 0.2
Partly Aged	0.82 ± 0.01	12.7 ± 0.3	0.52 ± 0.03	4.5 ± 0.2
Fully Aged	0.94 ± 0.01	12.8 ± 0.3	0.60 ± 0.03	5.1 ± 0.2

Xe-arc lamp. The device structure is: ITO 150 nm/ZnO 30 nm/PCE-10 : BT-CIC, 1 : 1.5, 80 nm/MoO_x 10 nm/Al 100 nm. The V_{80} experiences a significant increase of 0.4 V after 300 h, see inset. Fig. 9b shows the V_{off} and J_{sat} *vs.* time. The V_{off} drops by 0.15 V during aging, while the J_{sat} drops by 3.5 mA cm^{-2}. Fig. 9c shows the experimental (symbols) and fitted (lines) ΔBQE *vs.* V_{bulk}. The average V_{esc} is 0.2 V, corresponding to a site distance d = 10 nm. The fitted lines depart from the experimental data at large V_{bulk}, suggesting that the low trap site density assumption used to derive eqn (11) is invalid. The maximum values of ΔBQE *vs.* aging time are shown in Fig. 9d, where it is observed that the decrease in BQE saturates after 300 h.

Fig. 10a shows the BQE–V_{bulk} characteristics of an OPV with a C_{60}-SAM inserted at the ZnO/BHJ interface, and the inset shows the V_{80} *vs.* aging time. The BQE–V_{bulk}

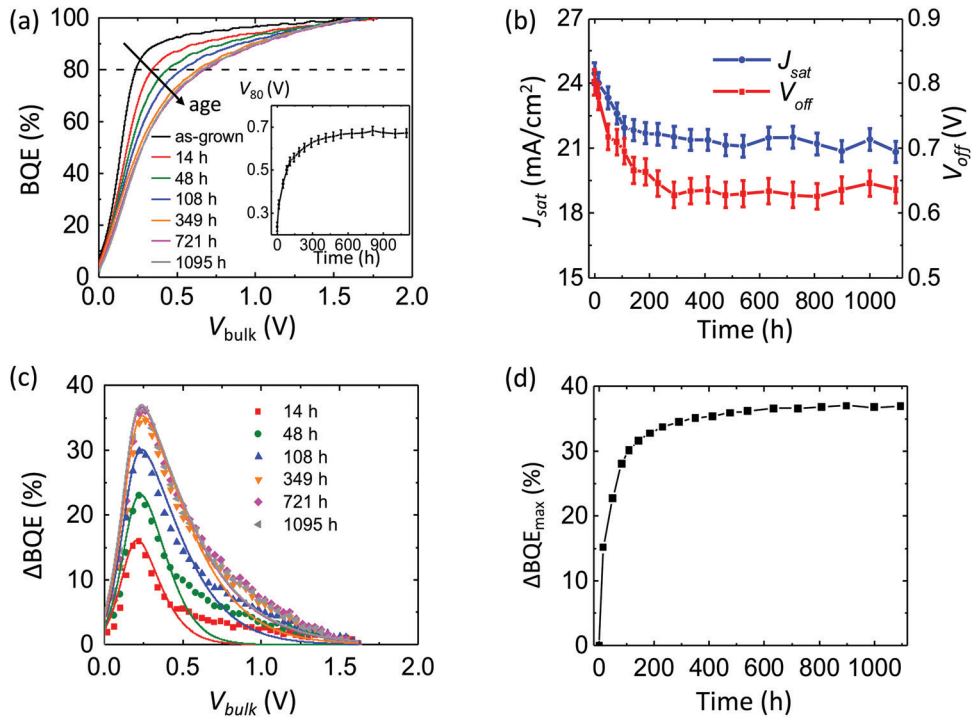

Fig. 9 (a) BQE–V_{bulk} characteristics of an inverted OPV with a PCE-10:BT-CIC BHJ and a ZnO CBL aged under simulated AM 1.5G illumination. Inset: V_{80} *vs.* aging time. (b) V_{off} and J_{sat} *vs.* aging time. (c) Experimental (symbols) and fitted (lines) decrease in BQE (ΔBQE) *vs.* V_{bulk} *vs.* aging time. (d) The maximum values of ΔBQE *vs.* aging time.

characteristics are stable after an initial burn-in. The V_{off} and J_{sat} *vs.* aging time is shown in Fig. 10b. The J_{sat} is stable, while V_{off} drops by 0.24 V.

4. Discussion

Conventional metrics used to analyze OPV performance such as V_{OC}, J_{SC} and FF often have entangled correlations with the device structure, making it difficult to evaluate the effectiveness of a particular layer in the photogeneration process. On the other hand, BQE, J_{sat} and V_{off}, can separate the BHJ properties from the edges. As shown in Fig. 3a, 4a, 5a and 6a, devices with different ABL, CBL or AIL layers have similar BQE–V_{bulk} characteristics. Indeed, the BQE–V_{bulk} characteristics are unaffected even for layers that severely reduce PCE (*e.g.*, WO_x ABLs and BPhen AILs) and BHJs with varying mixing ratios across the active region. The impacts of the contacts, buffer layers and interfaces are incorporated in V_{off} and J_{sat}, which depend on voltage drops and recombination at the edges, respectively. For clarification, the separation of the bulk properties from the edges is based on experimental observation, which is elucidated by the theory in Section 2.1. In cases when an energy barrier exists at one of the interfaces leading to a "S-shaped" *J–V* characteristics,[32] the BQE analysis is no longer able to separate the bulk properties from the edges (see ESI†). This failure is likely due to charge accumulation at the contact, causing V_{int} to have a large dependence on *V*.

Several mechanisms can lead to the degradation of OPV performance: morphological changes[33–35] or chemical changes (*e.g.*, photo-bleaching and molecule fragmentation)[29,36,37] in the BHJ, degradation of the electrodes,[38,39] degradation of the buffer layers,[40–43] chemical reactions and diffusion between BHJ and edge layers, *etc.*[44–47] As shown in Fig. 7a and b, the BQE of the DBP:C_{70} OPV decreases under illumination, whose trend can be fit with eqn (11), as shown in Fig. 7c. The V_{off} remains almost constant, suggesting that there is no significant increase in the voltage across the interface during aging. The J_{sat} experiences a decrease of 1 mA cm^{-2}, which may be due to increased trapping within the buffer layers.

In the partly aged device in Fig. 8a, only the lower section was exposed to illumination. This device has nearly identical BQE–V_{bulk} characteristics as the as-grown device, while the BQE of the fully aged device is reduced, as shown in Fig. 8b. This suggests that the MoO_x and the MoO_x/BHJ interface are not responsible for the decrease in BQE observed in Fig. 7a. The J_{sat} of the partly aged device is similar to that of the fully aged device, which is 0.5 mA cm^{-2} smaller than that of the as-grown device, as shown in Table 4, indicating that aging of the lower edge layers (nearest the substrate) account for the decrease in J_{sat} observed in Fig. 7b. The partly aged device has a V_{off} that is 0.12 V smaller compared with that of the as-grown and fully aged devices. This is possibly due to an energy barrier between the aged and unaged parts of the BHJ.

For solution-processed PCE-10:BT-CIC BHJs, the BQE decreases relative to the fresh device with a 0.4 V increase in V_{80} after 1000 h of aging under 1 sun intensity, simulated AM 1.5G illumination, as shown in Fig. 9a. The V_{off} drops by 0.15 V while J_{sat} decreases by 3.5 mA cm^{-2} (see Fig. 9b). The fitted lines depart from the experimental data at large V_{bulk} in Fig. 9c, suggesting the existence of trapped charges even at large V_{bulk}. This is possibly because a high trap site density results in multiple trapping events for each charge during charge extraction, increasing the recombination probability beyond that predicted by eqn (11) at large V_{bulk} (see P_{trap} in Table S3, ESI†). The ΔBQE saturates after 300 h, as shown in Fig. 9d.

To study whether the decrease in BQE is caused by changes in morphology or material decomposition in the BHJ,[34–37] or changes external to the active region such as photocatalytic reactions at the ZnO interface,[44,45] a C_{60}-SAM was inserted at the ZnO/BHJ interface to prevent interactions with the BHJ. With the C_{60}-SAM, the BQE decrease is eliminated except for a small burn-in effect, as shown in Fig. 10a. The OPV loss of efficiency with aging is, therefore, most likely due to chemical reactions between the BHJ and ZnO layer, while the BHJ itself appears to be stable. In addition, we heated the device in darkness at 45 °C and found that the BQE is not affected, while the V_{off} decreases (see ESI†).

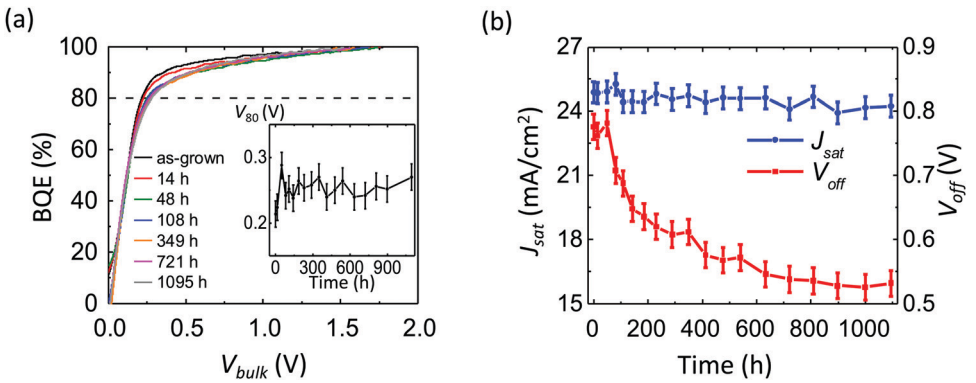

Fig. 10 (a) BQE–V_{bulk} characteristics of a PCE-10:BT-CIC OPV with a self-assembled monolayer (C_{60}-SAM) inserted between the BHJ and the ZnO layer under simulated AM 1.5G illumination. Inset: V_{80} *vs.* aging time. (b) V_{off} and J_{sat} *vs.* aging time.

5. Conclusions

In this work, we introduced a method to analyze OPV performance by directly measuring the charge photogeneration efficiency within the BHJ using the bulk quantum efficiency that is extracted directly from the OPV *J–V* characteristics. The BQE analysis was used to separate the properties of the BHJ from the device peripheral regions (interfaces, buffer layers, contacts) for both vacuum- and solution-processed OPVs. Compared with conventional metrics such as V_{OC}, J_{SC} and FF, the BQE, V_{off} and J_{sat}, introduced in this work are determined by either the active or the edge regions, providing physical insights into the photogeneration process. This method is derived for systems with localized charge carriers and isotropic dissociating interfaces, and thus might have broader applications such as for perovskite solar cells.

The BQE analysis is applied to quantitatively study degradation mechanisms in both vacuum and solution deposited devices. In solution-processed NFA OPVs, we show that the primary mechanism of performance degradation is induced by the ZnO buffer layer. By inserting a self-assembled monolayer at the BHJ/ZnO interface, the degradation is significantly suppressed and the BHJ is stabilized.

6. Experimental section

6.1 Device fabrication

All OPVs were fabricated on ITO coated glass substrates (Lumtec Corp.) with a sheet resistance of 15 Ω sq^{-1}. The ITO anodes were patterned into 2 mm wide strips. The substrates were cleaned using a detergent (tergitol solution) and solvents (acetone and isopropanol) and exposed to ultraviolet ozone for 10 min prior to thin film deposition.

For vacuum-processed OPVs, the substrates were transferred into a vacuum thermal evaporation (VTE) chamber with a base pressure of 10^{-7} torr, and all layers were deposited at rates between 0.2 to 1.6 Å s^{-1}. The deposition rates and thicknesses were measured using quartz crystal monitors and calibrated post-growth using variable-angle spectroscopic ellipsometry. Metal cathodes were deposited through 2 mm wide shadow mask openings oriented orthogonal to the ITO strips, forming device areas of 4 mm^2.

The ZnO CBL employed in solution-processed OPVs was spun onto the substrates at 4000 rpm for 1 min using a sol–gel ZnO precursor solution (Sigma-Aldrich Inc.), and then thermally annealed at 160 °C for 30 min in air. The SnO_2 CBL was deposited from a nanocrystal dispersion (Sigma-Aldrich Inc.). The SnO_2 dispersion was diluted to 0.4 wt% by adding isopropanol and spun onto the substrates at 4000 rpm for 1 min. The sample was then thermally annealed in air for 30 min at 160 °C. The C_{60}-SAM (1-Material Inc.) was dissolved at 1.5 mg mL^{-1} in chlorobenzene(CB) : tetrahydrofuran(THF) (2 : 1 vol%) solution and stirred at 300 rpm overnight. The solution was then spin-coated at 3500 rpm for 1 min, and thermally annealed at 110 °C for 10 min. A second spin-coating using CB : THF (2 : 1 vol%) solution spun at the same speed was applied on top of the film to remove residual C_{60}-SAM molecules that are not chemically bonded to the surface. The PCE10 : BT-CIC blend was dissolved at a total concentration of 16 mg mL^{-1} in 9 : 1 CB : chloroform solution with a 1 : 1.5 weight ratio, and stirred at 300 rpm overnight at 65 °C. The solution was subsequently spun onto the sample at 4000 rpm for 1 min. The AIL, MoO_x and Al cathode were deposited *via* the same procedures as the vacuum-processed OPVs.

For the devices in Fig. 7b, the MoO_x and the lower 10 nm of the BHJ were deposited on two identical ITO coated glass substrates in the VTE chamber and encapsulated in N_2 atmosphere. One sample (later fabricated into the partly aged device) was exposed to 27 suns for 17 days while the other (later fabricated into the as-grown device) was kept in darkness. Then both sample packages were opened and the remaining device layers including 44 nm thick BHJ, BPhen and Ag cathodes were deposited in the VTE chamber using the same procedures as the vacuum-processed OPVs. After the *J–V* measurement, the as-grown device was aged at 27 suns for 17 days which is referred to as the fully aged device.

6.2 Device aging and *J–V* measurement

The simulated solar illumination was produced using a large-area Xe-arc lamp filtered to approximate an AM 1.5G reference, and the intensity was calibrated to 1 sun intensity (1 kW m^{-2}) using a calibrated Si photodiode (National Renewable Energy Laboratory). The 27 suns white light source was achieved using high-intensity white LED arrays. The intensity was calibrated using the as-grown PCE-10:BT-CIC OPV in Fig. 8a. The OPV is illuminated using a solar simulator, and the J_{sc} is recorded as $J_{sc,AM1.5G}$. The OPV is then illuminated by the LED array with the intensity concentrated with a silver-coated reflective tube and a 10% transmissive neutral-density filter. The power of the LED array was adjusted so that the OPV produces a J_{sc} equivalent to $2.7J_{sc}$ at AM 1.5G. The details of the aging setup and the spectra of the light sources are found elsewhere.[29]

The *J–V* characteristics were measured inside a N_2 glovebox at room temperature using a semiconductor parameter analyzer (Agilent 4156C) with a 1 kW m^{-2} simulated AM 1.5G illumination source. Fluctuations in contact resistance during the *J–V* measurement results in randomness in the J_{ph} near V_{bulk} = 0. In this case, the V_{off} is determined by aligning the rising edges of the BQE–V_{bulk} curves (see ESI†).

Conflicts of interest

One of the authors (SRF) has an equity interest in a sponsor of this work (Universal Display Corp.). The conflict is under management by the University of Michigan Office of Research.

Acknowledgements

We thank Dr Shaocong Hou, Dr Dejiu Fan and Xinjing Huang for helpful discussions. This work was partially supported by the Department of the Navy, Office of Naval Research under

Award No. N00014-17-1-2211 (K. D., experiment and analysis, X. H., experiment, Y. L., experiment, S. R. F., analysis) and Universal Display Corporation.

References

1 R. R. Lunt, N. C. Giebink, A. A. Belak, J. B. Benziger and S. R. Forrest, *J. Appl. Phys.*, 2009, **105**, 053711.
2 G. Chen, H. Sasabe, Z. Wang, X.-F. Wang, Z. Hong, Y. Yang and J. Kido, *Adv. Mater.*, 2012, **24**, 2768.
3 R. Pandey, Y. Zou and R. J. Holmes, *Appl. Phys. Lett.*, 2012, **101**, 033308.
4 Y. Sun, G. C. Welch, W. L. Leong, C. J. Takacs, G. C. Bazan and A. J. Heeger, *Nat. Mater.*, 2012, **11**, 44.
5 T. S. van der Poll, J. A. Love, T.-Q. Nguyen and G. C. Bazan, *Adv. Mater.*, 2012, **24**, 3646.
6 J. J. M. Halls, C. A. Walsh, N. C. Greenham, E. A. Marseglia, R. H. Friend, S. C. Moratti and A. B. Holmes, *Nature*, 1995, **376**, 498.
7 G. Yu, J. Gao, J. C. Hummelen, F. Wudl and A. J. Heeger, *Science*, 1995, **270**, 1789.
8 H. Bässler, *Phys. Status Solidi B*, 1993, **175**, 15.
9 X. Liu, K. Ding, A. Panda and S. R. Forrest, *ACS Nano*, 2016, **10**, 7619.
10 K. Ding, X. Liu and S. R. Forrest, *Nano Lett.*, 2018, **18**, 3180.
11 Y. L. Lin, M. A. Fusella and B. P. Rand, *Adv. Energy Mater.*, 2018, **8**, 1702816.
12 A. A. Bakulin, A. Rao, V. G. Pavelyev, P. H. M. van Loosdrecht, M. S. Pshenichnikov, D. Niedzialek, J. Cornil, D. Beljonne and R. H. Friend, *Science*, 2012, **335**, 1340.
13 M.-H. Jao, H.-C. Liao and W.-F. Su, *J. Mater. Chem. A*, 2016, **4**, 5784.
14 B. Qi and J. Wang, *Phys. Chem. Chem. Phys.*, 2013, **15**, 8972.
15 R. A. J. Janssen and J. Nelson, *Adv. Mater.*, 2013, **25**, 1847.
16 N. K. Elumalai and A. Uddin, *Energy Environ. Sci.*, 2016, **9**, 391.
17 K. Vandewal, K. Tvingstedt, A. Gadisa, O. Inganäs and J. V. Manca, *Phys. Rev. B: Condens. Matter Mater. Phys.*, 2010, **81**, 125204.
18 L. J. A. Koster, V. D. Mihailetchi, H. Xie and P. W. M. Blom, *Appl. Phys. Lett.*, 2005, **87**, 203502.
19 K. Ding and S. R. Forrest, *Phys. Rev. Appl.*, 2020, **13**, 054046.
20 M. T. Greiner, M. G. Helander, W.-M. Tang, Z.-B. Wang, J. Qiu and Z.-H. Lu, *Nat. Mater.*, 2011, **11**, 76.
21 N. B. Kotadiya, H. Lu, A. Mondal, Y. Ie, D. Andrienko, P. W. M. Blom and G.-J. A. H. Wetzelaer, *Nat. Mater.*, 2018, **17**, 329.
22 K. Sotthewes, R. van Bremen, E. Dollekamp, T. Boulogne, K. Nowakowski, D. Kas, H. J. W. Zandvliet and P. Bampoulis, *J. Phys. Chem. C*, 2019, **123**, 5411.
23 D. Credgington, F. C. Jamieson, B. Walker, T.-Q. Nguyen and J. R. Durrant, *Adv. Mater.*, 2012, **24**, 2135.
24 T. Kirchartz, B. E. Pieters, J. Kirkpatrick, U. Rau and J. Nelson, *Phys. Rev. B: Condens. Matter Mater. Phys.*, 2011, **83**, 115209.
25 T. M. Clarke, A. Ballantyne, S. Shoaee, Y. W. Soon, W. Duffy, M. Heeney, I. McCulloch, J. Nelson and J. R. Durrant, *Adv. Mater.*, 2010, **22**, 5287.
26 A. K. K. Kyaw, D. H. Wang, V. Gupta, W. L. Leong, L. Ke, G. C. Bazan and A. J. Heeger, *ACS Nano*, 2013, **7**, 4569.
27 S. R. Cowan, R. A. Street, S. Cho and A. J. Heeger, *Phys. Rev. B: Condens. Matter Mater. Phys.*, 2011, **83**, 035205.
28 A. Miller and E. Abrahams, *Phys. Rev.*, 1960, **120**, 745.
29 Q. Burlingame, X. Huang, X. Liu, C. Jeong, C. Coburn and S. R. Forrest, *Nature*, 2019, **573**, 394.
30 X. Che, Y. Li, Y. Qu and S. R. Forrest, *Nat. Energy*, 2018, **3**, 422.
31 Y. Li, J.-D. Lin, X. Che, Y. Qu, F. Liu, L.-S. Liao and S. R. Forrest, *J. Am. Chem. Soc.*, 2017, **139**, 17114.
32 A. Sundqvist, O. J. Sandberg, M. Nyman, J.-H. Smått and R. Österbacka, *Adv. Energy Mater.*, 2016, **6**, 1502265.
33 M. Jørgensen, K. Norrman and F. C. Krebs, *Sol. Energy Mater. Sol. Cells*, 2008, **92**, 686.
34 B. Ray and M. A. Alam, *Appl. Phys. Lett.*, 2011, **99**, 033303.
35 W. R. Mateker and M. D. McGehee, *Adv. Mater.*, 2017, **29**, 1603940.
36 M. O. Reese, A. M. Nardes, B. L. Rupert, R. E. Larsen, D. C. Olson, M. T. Lloyd, S. E. Shaheen, D. S. Ginley, G. Rumbles and N. Kopidakis, *Adv. Funct. Mater.*, 2010, **20**, 3476.
37 W. R. Mateker, T. Heumueller, R. Cheacharoen, I. T. Sachs-Quintana, M. D. McGehee, J. Warnan, P. M. Beaujuge, X. Liu and G. C. Bazan, *Chem. Mater.*, 2015, **27**, 6345.
38 S. Cros, M. Firon, S. Lenfant, P. Trouslard and L. Beck, *Nucl. Instrum. Methods Phys. Res., Sect. B*, 2006, **251**, 257.
39 F. So and D. Kondakov, *Adv. Mater.*, 2010, **22**, 3762.
40 E. Bovill, N. Scarratt, J. Griffin, H. Yi, A. Iraqi, A. R. Buckley, J. W. Kingsley and D. G. Lidzey, *Appl. Phys. Lett.*, 2015, **106**, 073301.
41 R. Rösch, D. M. Tanenbaum, M. Jørgensen, M. Seeland, M. Bärenklau, M. Hermenau, E. Voroshazi, M. T. Lloyd, Y. Galagan, B. Zimmermann, U. Würfel, M. Hösel, H. F. Dam, S. A. Gevorgyan, S. Kudret, W. Maes, L. Lutsen, D. Vanderzande, R. Andriessen, G. Teran-Escobar, M. Lira-Cantu, A. Rivaton, G. Y. Uzunoğlu, D. Germack, B. Andreasen, M. V. Madsen, K. Norrman, H. Hoppe and F. C. Krebs, *Energy Environ. Sci.*, 2012, **5**, 6521.
42 A. Manor, E. A. Katz, T. Tromholt and F. C. Krebs, *Adv. Energy Mater.*, 2011, **1**, 836.
43 S. Trost, T. Becker, A. Polywka, P. Görrn, M. F. Oszajca, N. A. Luechinger, D. Rogalla, M. Weidner, P. Reckers, T. Mayer and T. Riedl, *Adv. Energy Mater.*, 2016, **6**, 1600347.
44 S. Park and H. J. Son, *J. Mater. Chem. A*, 2019, **7**, 25830.
45 Y. Jiang, L. Sun, F. Jiang, C. Xie, L. Hu, X. Dong, F. Qin, T. Liu, L. Hu, X. Jiang and Y. Zhou, *Mater. Horiz.*, 2019, **6**, 1438.
46 J. Li, Q. Dong, N. Li and L. Wang, *Adv. Energy Mater.*, 2017, **7**, 1602922.
47 B. P. Rand, P. Peumans and S. R. Forrest, *J. Appl. Phys.*, 2004, **96**, 7519.